ADVANCED MATERIALS
www.advmat.de

# Mixed-Metal Promotion in a Manganese-Molybdenum Oxynitride as Catalyst to Integrate C—C and C—N Coupling Reactions for the Direct Synthesis of Acetonitrile from Syngas and Ammonia

*M. Elena Martínez-Monje, Wilson Henao, Tania Rodenas, Patricia Concepción, Virginia Pérez Dieste, Alexander Missyul, Giovanni Agostini, and Gonzalo Prieto**

**Transition metal nitrides and their oxy- and carbo-nitride analogues attract interest as catalysts in various sustainability areas. They offer potential in the development of conversion routes for the synthesis of nitrogenated organic compounds, via the integration of C—C and C—N coupling reactions from sustainable $C_1$ and $N_1$ feedstocks, linking carbon and nitrogen renewable cycles. Herein, a series of structurally uniform $(NH_4)nH_mM_xM_{oy}O_z{\cdot}2H_2O$ ammonium metal molybdate materials (*C 2/m*) serve as catalyst precursors, providing atomic-level metal mixing. Among various 3d transition metals, Mn proves the most effective promoter. A [MnMo] mixed-metal catalyst exhibits superior selectivity to acetonitrile (56 % among all organic products) and stability, significantly outperforming monometallic [Mo] and [Mn] counterparts. Multimodal physicochemical characterization, including temperature-resolved X-ray diffraction, Xray absorption near-edge structure and extended X-ray absorption fine structure, and depth-profiling X-ray photoelectron spectroscopy, shows partial nitridation to a cubic (*Fm-3m*) mixed-metal oxynitride as the working catalyst under operation conditions. Consistent with first-principles thermochemistry, manganese is found to disrupt extended molybdenum nitride domains, preserving manganese-enriched oxynitride domains under the markedly nitriding reaction conditions. Density functional theory predicts these partially oxidic domains to facilitate C—C coupling reactions compared to fully nitrided surfaces, enhancing conversion of the stable reaction intermediate HCN to acetonitrile.**

## 1. Introduction

Transition metal nitrides, and their oxy- and carbo-nitride analogues, offer interesting properties as catalysts in a wide array of emerging chemical technologies associated to the transition toward a more sustainable energy and chemical sectors.[1–5] Accessible via a wide array of synthesis routes,[6–8] the unique combination of thermal stability, electronic conductivity, and tunable surface reactivity makes this class of compounds particularly interesting and versatile materials as solid catalysts for transformations driven (photo)thermally, as well as by means of electrical bias.[9–12] Their capacity to integrate bifunctional Lewis acid-base sites on their surface is of interest to facilitate the activation of small, recalcitrant molecules like $CO_2$, $N_2$, and light hydrocarbons.[13–15] Moreover, their compositional versatility offers a blueprint toward catalyst formulations with reduced reliance on scarce (precious) or toxic elements. Indeed, transition metal nitrides bear peculiar surface electronic and catalytic features, which resemble those of group VIII elements in metallic form.[16–18]

M. E. Martínez-Monje, W. Henao, T. Rodenas, P. Concepción, G. Prieto
ITQ Instituto de Tecnología Química
Universitat Politècnica de València-Consejo Superior de Investigaciones Científicas (UPV-CSIC)
Avenida de los Naranjos s/n, Valencia 46022, Spain
E-mail: prieto@itq.upv.es

V. P. Dieste, A. Missyul, G. Agostini
ALBA Synchrotron Light Source
Carrer de la Llum 2–26, Cerdanyola del Vallès, Barcelona 08290, Spain

The ORCID identification number(s) for the author(s) of this article can be found under https://doi.org/10.1002/adma.202506973



**DOI: 10.1002/adma.202506973**

Besides, they are known to withstand aggressive reaction conditions in the presence of gaseous ammonia[19–21] and, under certain conditions, have been proposed to act as reservoirs and solid transfer agents for active nitrogen species.[22,23] These characteristics position transition metal nitrides, and their oxy- and carbo-nitride correspondents, as remarkably adaptable and resilient platforms for environmentally friendly, next-generation catalytic and energy conversion/storage processes.

Over the last two decades, significant progress has been witnessed toward the consolidation of carbon and nitrogen renewable cycles, disconnected from resources and energy forms of fossil origin.[24,25] The coupling of these independent chemical cycles, via the development of versatile conversion routes for the formation of carbon-nitrogen bonds from unconventional, for example, $C_1$ and $N_1$, feedstocks is an attractive strategy toward the sustainable production of nitrogen-containing organic compounds, which are ubiquitous in a plethora of applications, from fine chemistry to textiles and polymer production.

In particular, aliphatic nitriles are essential building blocks for the manufacture of perfumes, pesticides, polymers and pharmaceuticals, as well as widely applied as liquid solvents for solutes of a wide range of polarity. At present, industrial nitrile production is dominated by ammoxidation[26] and hydrocyanation[27] routes from high added-value olefin or oxygenate compounds. Therefore, alternative routes for a direct synthesis of aliphatic nitriles from cheap and abundant raw materials is highly sought. A direct alkane ammo-dehydrogenation has been reported on bifunctional metal-acid catalysts.[28] This route proved highly selective to produce acetonitrile (MeCN) from ethane and ammonia mixtures, although alkane dehydrogenation equilibria under reductive conditions limit the yield attainable per reactor pass. The direct conversion of mixtures of syngas ($CO + H_2$) and ammonia is particularly appealing, as it widens the feedstock scope to essentially any carbonaceous raw material. Potentially, the latter opens the door to a fully renewable nitrile production when integrated into emerging biomass- or power-to-syngas[29] and power-to-ammonia[30] technologies.

Nitrile production from syngas and ammonia mixtures requires concerted mechanisms for CO hydrogenation as well as C—C and C—N coupling reactions, respectively. Attempts to engage ammonia as a nitrogen source in syngas conversion catalysis date back several decades. Addition of $NH_3$ to a methanol synthesis process on a promoted copper chromite catalyst led to nearly quantitative selectivities to methylamines.[31,32] Later, co-feeding of ammonia to Fischer-Tropsch (FT) catalysts was explored as a means to produce $C_{2+}$ nitrogenated compounds. Typically, an unselective range of terminal aliphatic nitro-compounds (amines, nitriles, amides) was observed, along with regular *n*-hydrocarbons, under FT-standard reaction temperatures (443–573 K).[33–36] Experimental evidences suggested that nitrogenated products were produced at the expense of oxygenates upon the addition of ammonia to the gas feed.[36,37] High selectivities to nitrile products, particularly acetonitrile, were reported at higher operation temperatures (>673 K) by researchers at Monsanto[38] and others[39–41] using supported Mo and Fe catalysts. However, long-term stability proved a challenge and decays in nitrile production rates of >50 % over a few hours on stream were observed for both Fe-based[41] and Mo[39]-based catalysts.

Common to both Fe and Mo-based catalysts is that they can form a variety of (interstitial) carbide, nitride and mixed carbo-nitride compounds. Unlike in the case of Fischer-Tropsch catalysts based on Co, Ru or Rh, which are active in their metallic state, for Fe and Mo, carbide and nitride compounds have been conclusively shown to be the catalytically active forms for syngas conversion reactions.[42–45] With standard $CO/H_2$ syngas feeds, an initial transient restructuring of oxidic or metallic catalyst precursors has been shown to occur, developing in situ active carbidic species.[43–46] Under those $CO/H_2/NH_3$ atmospheres applied for the direct synthesis of nitrogen-containing compounds, contact with an additional reactive source of nitrogen broadens the catalyst speciation possibilities significantly. As a result, and despite its fundamental significance in advancing toward optimal performances, the nature of the catalyst species responsible for a direct conversion of ammonia-syngas feeds to nitrile compounds remains an unresolved question. In previous studies, fundamentally different phenomena, such as fast decomposition of nitride species into the corresponding carbide compounds,[41] as well as metal oxide crystallite sintering,[39] have been proposed to take place under reaction conditions and connected to catalyst deactivation.

Herein we investigate a [MnMo] mixed-metal oxynitride material as a catalyst for the direct production of acetonitrile from ammonia-syngas mixtures with remarkable selectivity and stability. Multi-modal temperature- and time-resolved characterizations, coupled with quantum mechanics DFT simulations, offer insights into the development of the working catalyst under reaction conditions, and the reaction mechanism. The co-existence of Mn and Mo in the active catalyst brings about a synergetic effect which is responsible for a notably enhanced catalytic performance compared to either of the monometallic counterparts.

## 2. Results and Discussion

To investigate mixed-metal effects in molybdenum-based catalyst materials, a series of crystalline ammonium M (II) molybdate materials (M = Zn, Cu, Ni, Co or Mn) were synthesized via a co-precipitation route and applied as catalyst precursors (see Experimental Section for details on the synthesis of this set of materials). The series of as-synthesized mixed-metal catalyst precursor materials showed experimental bulk M:Mo ratios, determined by Inductively-Coupled Plasma-Optical Emission Spectroscopy (ICP-OES)a, of 1.2 ± 0.2 (atomic), in fair agreement with the nominal equimolar content (Table S1, Supporting Information). In all cases, the solids showed highly crystalline structures. As shown in **Figure 1**, these materials showed average primary crystal sizes >0.5 µm. Moreover, crystal morphology depended markedly on the nature of the divalent cation ($M^{2+}$), spanning from polyhedral crystals for [MnMo], to platelet crystals for [NiMo], or desert-rose morphologies in the case of [CoMo], [CuMo], and [ZnMo]. In the case of [NiMo], a minor population of sub-µm sized crystals with ill-defined shape appeared accompanying the dominant population of larger plate-like crystals. X-ray diffractograms could be indexed to ammonium metal molybdates (monoclinic, *C 2/m*) of general formula $(NH_4)_nH_mM_xMo_yO_z{\cdot}2H_2O$. In these structures, $M^{2+}$ and $Mo^{6+}$ cations occupy octahedral ($O_h$) and tetrahedral ($T_h$)

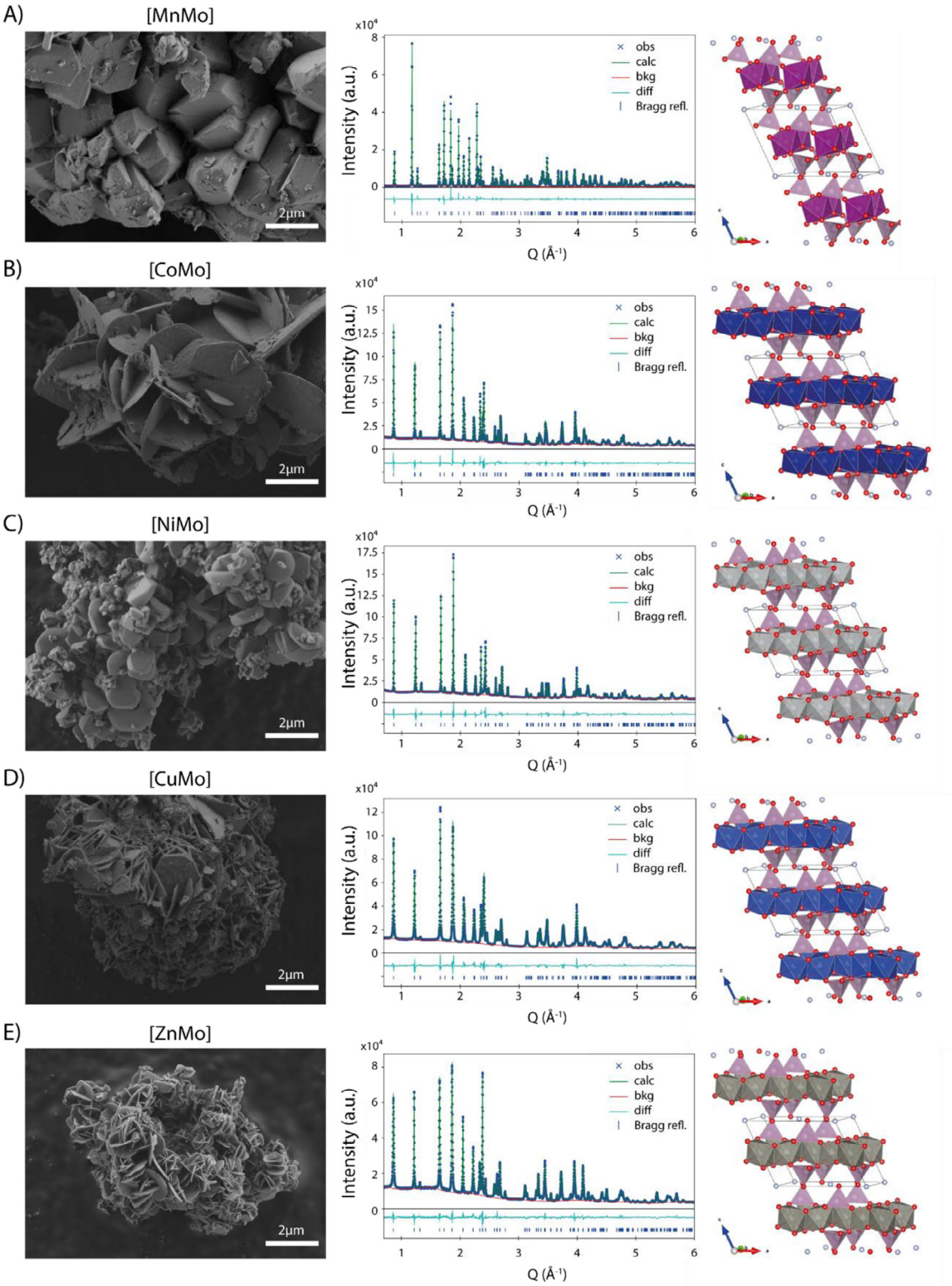


**Figure 1.** Representative field-emission scanning electron microscopy (FE-SEM) micrographs (left) and Rietveld refinement of powder X-ray diffraction patterns (right), for the series of A) [MnMo], B) [CoMo], C) [NiMo], D) [CuMo] and E) [ZnMo] mixed-metal ammonium molybdate catalyst precursors. XRD profiles include experimental data (blue cross), calculated pattern (green line), simulated background (red line), residual profile (bottom light blue line), and position of Bragg reflections (bottom dark blue lines). In the structural models, tetrahedra enclosing $Mo^{+6}$ cations are depicted in pale pink, whereas octahedra enclosing $M^{+2}$ cations (M = Mn, Co, Ni, Cu or Zn) as shown in gray, blue or magenta grades. Oxygen atoms are shown in red, and nitrogen atoms in $NH_4^+$ cations are shown in white. For simplicity, no H atoms are depicted.

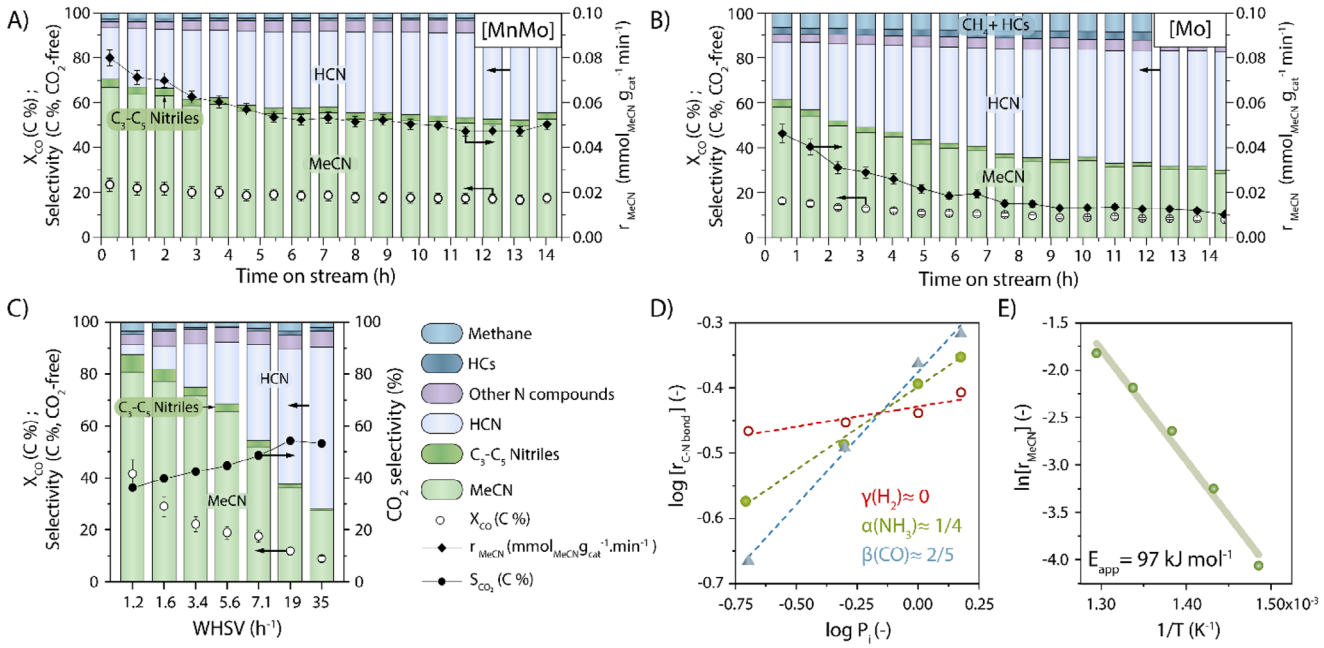


**Figure 2.** Evolution of CO conversion ($X_{CO}$), product selectivity ($CO_2$-free basis) and acetonitrile formation rate ($r_{MeCN}$) with time-on-stream (TOS) for the comparative A) [MnMo] mixed-metal and B) [Mo] monometallic catalysts in the direct conversion of syngas/ammonia mixtures (WHSV = 7.1 $h^{-1}$); C) dependence of CO conversion and product selectivity ($CO_2$-free basis) with WHSV over the [MnMo] mixed-metal catalyst. Reaction conditions: $T$ = 723 K, $P$ = 3 bar, gas feed molar composition $NH_3$:CO:$H_2$ = 2:1:1. The error bars added to the scatter symbols on the plot represent the standard error of the mean as determined from independent repetition tests for [MnMo] ($n$ = 4) and [Mo] ($n$ = 2), respectively. The corresponding standard error of the mean for selectivity to major reaction products, that is, MeCN and HCN were <4.8% for [MnMo] and <4.3% for [Mo], respectively; D) Log-plot for the C—N bond forward formation rate dependence with the partial pressure of $NH_3$ (green, solid circles and dashed line), CO (blue, solid triangles and dashed line) and $H_2$ (red, open circles and dashed line) reactants in the feed over the [MnMo] catalyst. The corresponding apparent reaction orders $\alpha(NH_3)$, $\beta(CO)$ and $\gamma(H_2)$ are indicated on the figure. E) Experimental Arrhenius plot for the [MnMo] catalyst in the direct conversion of syngas/ammonia mixtures. Reaction conditions: $T$ = 723 K, $P$ = 3 bar, gas feed molar composition $NH_3$:CO:$H_2$ = 2:1:1, $X_{CO}$ ≤12 %. In the legend: *HCs* refers to $C_{2+}$ hydrocarbons, lacking heteroatoms. Primarily $C_2$ hydrocarbons (0.4–0.6%) and $C_3$ hydrocarbons (0.3–0.5%) were detected in this minority product slate. *Other N compounds* refers to nitrogenated organic compounds other than HCN and nitriles. Primarily methylamine (3.7–5.3%) and pyrroles (0.1–1.3%) were detected in this minority product slate.

crystallographic positions, respectively, providing atomic-level metal mixing as starting point for compositionally uniform catalysts.

Assessment of the series of [MMo] materials as catalysts for the direct conversion of syngas and ammonia mixtures revealed that the [MnMo] mixed-metal catalyst outperformed others in selectively and stably producing acetonitrile (Figure S1, Table S2, Supporting Information). Alternative catalysts showed modest (<30%) selectivity to acetonitrile (MeCN) within the organic products, and/or underwent a marked deactivation, with acetonitrile production rates declining by 50–90% within the first ≈9 h on-stream, compared to a 37.5% decline for [MnMo]. Particularly, [NiMo] exhibited a very high CO conversion rate, which translated into a high formation rate of acetonitrile (Figure S1, Supporting Information). However, extensive methanation activity ($S_{CH4}$ of 54.3%, Table S2, Supporting Information), attributed to the reductive agglomeration of nickel and its spatial segregation from the mixed-metal system into $Ni^0$ crystallites (Figure S2, Supporting Information) resulted in a very modest selectivity to MeCN (<20% within the organic products) under the tested conditions. Consequently, further analyses concentrated on understanding the promotional effect of manganese in the [MnMo] mixed-metal material, particularly in comparison to a reference monometallic $MoO_3$ catalyst, hereafter referred to as [Mo].[47]

The catalytic performance of the [MnMo] catalyst is summarized in **Figure 2A**. Following an initial decay in activity, particularly over the first ≈4–5 h on-stream, a pseudo-steady was reached under the applied reaction conditions ($T$ = 723 K, $P$ = 3 bar, $WHSV$ = 7.1 $h^{-1}$), beyond which point CO conversion remained remarkably stable up to at least 14 h on-stream, with a decline rate <1.9 % $h^{-1}$. Nitriles prevailed among the organic products. In this product fraction, the selectivity to acetonitrile declined from an initial 66.8 % to level off at 56.1 % after ≈5 h on-stream, resulting in a steady acetonitrile production rate of ≈$5{\cdot}10^{-2}$ mmol $g_{cat}^{-1}$ $min^{-1}$ at longer reaction times. Hydrogen cyanide (HCN) was detected as the predominant remaining organic product, alongside minor amounts of methane and other light ($C_2$-$_6$) hydrocarbons (3.3 %) and additional nitrogen compounds, primarily methylamine (5.4 %). A fraction of the oxygen in the syngas feed was rejected in the form of $CO_2$, via the water gas shift reaction (WGSR), with the selectivity to $CO_2$ being 48.4 % under steady state.

The [MnMo] mixed-metal catalyst was evidently superior to either monometallic counterpart. The [Mo] catalyst exhibited a more pronounced decline in acetonitrile formation rate during the initial ≈9 h on-stream (Figure 2B), eventually stabilizing at a pseudo-steady acetonitrile production rate of $13{\cdot}10^{-3}$ mmol $g_{cat}^{-1}$ $min^{-1}$, circa fourfold lower than for the [MnMo] catalyst,

and delivered a reduced selectivity to acetonitrile of 31.6 %. In this case, HCN emerged as the primary organic product, suggesting an intrinsic limitation of the [Mo] catalyst in driving C–C coupling reactions. Comparatively similar results were obtained if $(NH_4)_6Mo_7O_{24}{\cdot}4H_2O$ was applied as precursor for the monometallic, molybdenum-based catalyst, in analogy to the ammonium molybdate nature of the mixed-metal catalyst precursors (Figure S3, Supporting Information). Also in this case, a greater activity decay and significantly lower selectivity to nitriles where registered compared to [MnMo]. Therefore, considering the similar performance, $MoO_3$ is hereafter consider as the precursor for the [Mo] material reference compound, as it provided a more consistent basis for comparison with the monometallic [Mn] counterpart, for which the use of ammonium permanganate ($NH_4MnO_4$) as a precursor was ruled out due to its hazardous (explosive) nature upon heating and dehydration. Hence, $Mn_2O_3$ was applied as catalyst precursor for the [Mn], monometallic reference. This material yielded only a very modest acetonitrile production rate ($3{\cdot}10^{-3}$ mmol $g_{cat}^{-1}$ $min^{-1}$) and selectivity (23.4 %) at the same reaction conditions (Figure S4, Supporting Information).

An assessment of the performance of the [MnMo] catalyst at different space velocities, thus different CO conversion levels, revealed a marked and progressive shift in the selectivity pattern (Figure 2C). While HCN dominated at shorter contact times, acetonitrile progressively became the major organic product at higher contact times, supporting the notion that HCN is a primary product, which engages further in C—C coupling to $C_{2+}$ nitriles.[48] Similar trends, albeit at significantly poorer activity levels, were observed for the corresponding monometallic catalysts (Figures S4 and S5, Supporting Information). On [MnMo], both $NH_3$ and CO reactants showed positive reaction orders of ≈1/4 and 2/5, respectively, for C—N coupling. Moreover, the reaction was determined to be essentially zero order with respect to $H_2$, indicating a high surface site occupancy by $H^*$ species under working conditions (Figure 2D). The apparent activation energy ($E_{app}$) for acetonitrile formation was 97 kJ $mol^{-1}$ (Figure 2E), that is, significantly lower than for the monometallic [Mo] counterpart catalyst (151 kJ $mol^{-1}$).[47] Moreover, nitrile products obeyed an Anderson-Schulz-Flory (ASF) distribution, indicative of a chain-propagation mechanism (Figure S6, Supporting Information). The chain growth probability for nitrile synthesis was 0.30 ± 0.02, regardless of catalyst composition ([Mo], [Mn], or [MnMo]). This consistency suggests mechanistic similarities in the C–C coupling process across catalysts, predominantly yielding $C_2$–$C_3$ nitriles, with acetonitrile as the main product.

Transient analysis of the formation rates of HCN and acetonitrile on $MnMoO_4$, the product of thermal decomposition of the ammonium mangano molybdate catalyst precursor (vide infra), revealed that HCN formed immediately at the onset of the reaction, whereas acetonitrile formation was delayed by a ≈10 min induction period (Figure S7, Supporting Information). These findings suggest that the catalyst undergoes structural reorganization upon exposure to reaction conditions, leading to the in situ development of an active phase responsible for HCN activation and further C–C coupling to form $C_{2+}$ nitriles. Therefore, we have adopted a multi-technique approach to assess the dynamic structural evolution and resting state of the [MnMo] catalyst material under reaction conditions.

Rietveld refinement analysis for the [MnMo] ammonium mangano molybdate catalyst precursor revealed site occupancies for $Mn^{2+}$ ($O_h$) and $Mo^{6+}$ ($T_h$) of 0.955(2) and 1, at the fractional atomic coordinates (1/4, 1/4, 1/2) and (0.58261(7), 0.0, 0.78307(8)), respectively (Figure S8A, Supporting Information). In addition, temperature-resolved X-ray diffractograms were registered on exposure of this precursor material to flow of the reactive gas atmosphere. At ≈475 K, the crystalline starting material decomposed, yielding a transient, intermediate crystal phase which could not be identified (Figure S8B, Supporting Information). Further heating to 598 K resulted in the formation of the monoclinic $MnMoO_4$ mixed oxide (*C12/m1*, ICSD 15615). Finally, an additional phase transition occurred at ≈773 K, producing a new cubic phase (*Fm-3m*) characterized by weaker and broader diffraction peaks, indicating smaller crystalline domains. An essentially identical final diffractogram was observed after exposure of the catalyst to reaction conditions at the standard operating temperature of 723 K for over 60 and 600 min (Figure S9, Supporting Information), suggesting that this structure represents the resting state of the in situ developed active catalyst.

Temperature-resolved analysis of the bulk compositional evolution showed, first, a decline in the nitrogen content from 2.7 wt% to 0.5 wt% up to 673 K, in correspondence with the decomposition of the starting ammonium mangano molybdate material into the $MnMoO_4$ mixed-metal oxide (Figure S10, Supporting Information). At higher temperatures, significant nitrogen uptake set in, and increased with temperature to reach 5.4 N wt% at 873 K, confirming oxide nitridation. Carbon uptake was also observed at temperatures ≥723 K, albeit at notably lower contents up to 0.5 C wt%. Extended isothermal exposure to reaction conditions at 723 K led to increments in N and C contents, reaching 4.4 wt% N and 1.0 wt% C after 60 min, and essentially stabilizing up to 600 min on-stream. Consistent with the catalyst's performance over time (Figure 2A), these results suggest that a stable composition was achieved for the active catalyst. Notably, the pseudo-steady bulk N and C levels were lower in [MnMo] (4.8 and 1.1 wt%, respectively) than in either monometallic counterpart (8.5 N wt%, 2.3 C wt% and 14.9 N wt%, 7.6 C wt% for [Mo] and [Mn] catalysts, respectively, Figure S10, Supporting Information).

Complementarily, the development of the catalyst phase during exposure to reaction conditions was investigated with near-surface resolution using depth profiling synchrotron radiation X-ray phoelectron spectroscopy (SR-XPS), via the modulation of the incident photon energy in the range of 400–750 eV. **Figure 3A** summarizes the speciation of molybdenum, determined by analyzing the Mo3d core-level after ex situ exposure to process conditions for different times on-stream. Four different Mo species were discriminated, which have been ascribed to $Mo^{6+}$ (232.2 ± 0.2 eV), $Mo^{5+}$ (230.8 ± 0.2 eV), and $Mo^{4+}$ (229.5 ± 0.1 eV) in oxide compounds, and $Mo^{4+}$ in nitride compounds (228.9 ± 0.1 eV),[49] respectively, in order of increasing metal reduction degree. Metal oxide nitridation was found to proceed swiftly under reaction conditions. As illustrated in Figure 3B, already after 10 min on-stream, about 50 % of the near-surface Mo atoms had been reduced to lower valent $Mo^{4+}$. Further reduction and nitridation were evident after 60 min. Beyond this time-on-stream, changes in Mo speciation were only minor up to 600 min

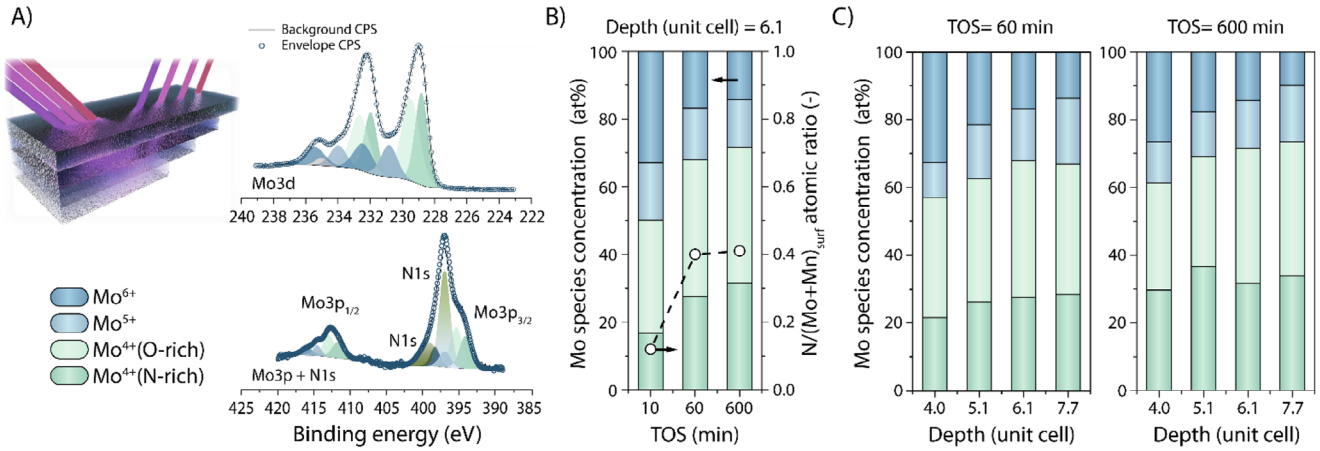


**Figure 3.** A) Illustration of synchrotron radiation X-ray photoelectron spectroscopy (SR-XPS) near-surface depth compositional profiling on powder solids upon modulation of the energy of the irradiating X-ray beam, and exemplary deconvolution analysis of Mo3d and Mo3p+N1s core level spectral regions for the [MnMo] catalyst following exposure to reaction conditions at 723 K for 600 min; B) Evolution of the near-surface relative abundance of molybdenum species and the N/Mo atomic ratio on the [MnMo] catalyst with time-on-stream (TOS) under reaction conditions at 723 K. Data correspond to an analysis depth of 2.6 nm, equivalent to ≈6 *Fm-3m* unit cells (incident X-ray energy of 600 eV); C) Evolution of molybdenum speciation with the photoemission analysis depth for the [MnMo] catalyst, following exposure to reaction conditions at 723 K for 60 min (left) and 600 min (right) time-on-stream.

on-stream, while the near-surface N-to-metal atomic ratio stabilized at ≈0.4, indicating a steady surface nitridation degree.

Depth profiling analysis of the catalyst after exposure for 60 min to reaction conditions revealed a gradient in Mo speciation, showing a decreasing degree of reduction toward the outer surface. This depth-profiling evolution was qualitatively maintained after 600 min, albeit at slightly higher overall near-surface Mo reduction extents. Progressively higher contributions from lower valent Mo were detected with increasing analysis depth, while the concentration of $Mo^{5+/6+}$ species was the highest (38.6 %) closest to the top surface. These findings suggest that an overall less nitrified (more oxidized) metal state is preserved on the catalyst's outermost surface, likely driven by the presence of water or $CO_2$ mild oxidants produced as side-products under reaction conditions, particularly once the driving force for nitridation has diminished.

The coexistence of Mn and Mo in the catalyst composition led to lower near-surface nitrogen contents after prolonged exposure to reaction conditions. Using laboratory-based XPS with a fixed incident photon energy of 1486.6 eV (Al K$\alpha$ line), that is, providing an analysis depth two to three times greater than SR-XPS, the near-surface N-to-metal atomic ratio for [MnMo] was approximately half (0.72) of that determined for the [Mo] and [Mn] catalysts (1.34 and 1.47, respectively; Table S3, Supporting Information). This indicates an overall lower surface nitridation effect in the Mn-Mo mixed-metal catalyst.

N1s photoemission analysis indicated near-surface nitrogen species with binding energies (BEs) of 397.0 ± 0.3 eV and 399.2 ± 0.2 eV, consistent with metal nitrides and partially hydrogenated nitrogen species in oxide environments, for example, $MO_x(NH_2)_y$, respectively.[49] The [MnMo] mixed-metal catalyst exhibited a higher relative contribution from the latter. In the C1s region, carbon species were identified with BEs of 284.6 eV, linked to graphitic or adventitious carbon. Contributions with BEs of 286.1 ± 0.3 eV and 288.5±0.8 eV were also discerned. The former signifies the presence of adsorbates with C—N bonding,[50] while the latter may be associated to surface carbonate species,[51] respectively. No signs for carbidic carbon species (BE ≈ 282.7 eV) were detected, ruling out any significant carbidization of the material under reaction conditions. Combined, the results from bulk and near-surface compositional analyses indicate a substantial incorporation of nitrogen atoms, though not carbon, into the structure of the mixed-metal material under reaction settings. Additionally, a synergistic interaction between manganese (Mn) and molybdenum (Mo) appears to limit the extent of catalyst surface nitridation under working conditions.

Temperature-resolved X-ray absorption near-edge structure (XANES) spectroscopy provided further insights into the evolution of the formal oxidation state (OS) and coordination geometry for Mo and Mn metals during the in situ development of the active catalyst phase (**Figure 4**, Table S4, Supporting Information).

A systematic decrease in the Mo-K edge energy reflected a progressive decrease in the average $OS_{Mo}$ on increasing temperature, from 6.2 in the $(NH_4)_2H_2Mn_4Mo_4O_{18}{\cdot}2H_2O$ precursor to 4.1 at 873 K, that is, similar to that in a $\gamma$-$Mo_2N$ standard and thus compatible with in situ nitridation (Figure 4A). A qualitatively similar behavior was observed for the [Mo] monometallic counterpart, which underwent nitridation to $\gamma$-$MoN_x$ under process conditions (Figure S11, Supporting Information). Noticeably, the presence of Mn in the mixed-metal catalyst caused a significant delay in the reduction of Mo compared to the monometallic [Mo] catalyst at temperatures below 750 K (Figure 4C). Along with molybdenum reduction, a progressive dampening and eventual disappearance of the pre-edge feature in the XANES spectra suggested the evolution from a tetrahedral ($T_h$) Mo coordination in the catalyst precursor to a more centrosymmetric octahedral coordination environment in the final active material (Figure 4D). In contrast, increasing temperatures under the reaction atmosphere resulted in an increase in the Mn-K edge energy,

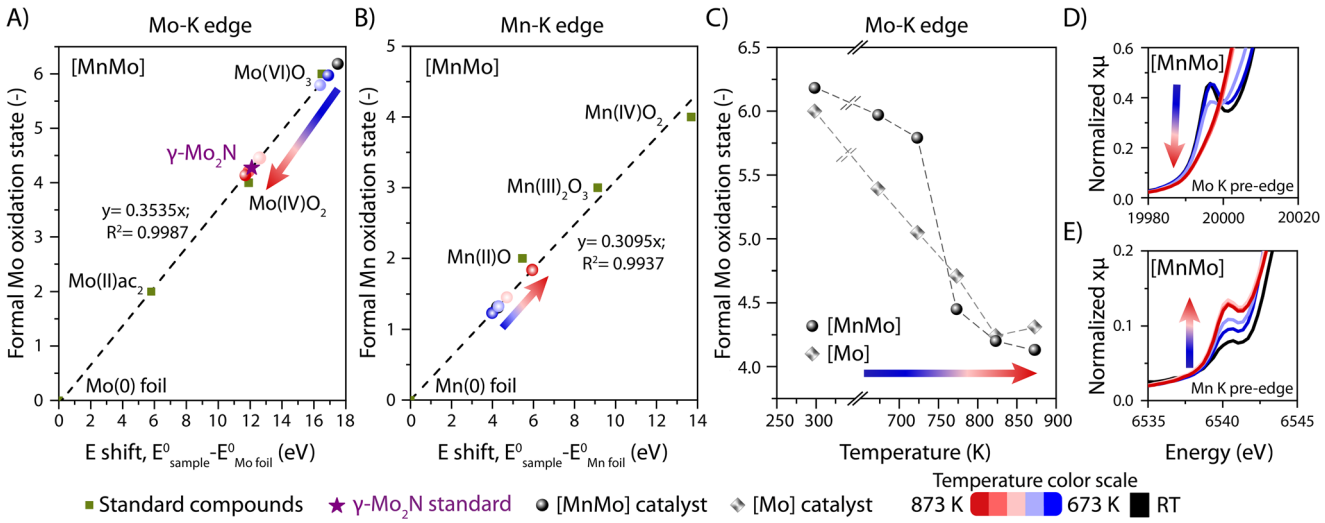


**Figure 4.** Evolution of the average formal oxidation state for A) Mo ($OS_{Mo}$) and B) Mn ($OS_{Mn}$), respectively, as derived from the analysis of the energy shift for Mo-K and Mn-K XANES edge energies with respect to the corresponding metallic foil ($E^0_{sample}$-$E^{\circ}_{foil}$), as a result of exposure of the [MnMo] precursor to reaction conditions at increasing temperatures. Green square data points correspond to the series of standard pure compounds with known Mo ($OS_{Mo}$) and Mn ($OS_{Mn}$) oxidation states. The dashed line corresponds to the linear regression for those data points determined for the standard compounds. C) Comparison of the evolution of the $OS_{Mo}$ with temperature for the [MnMo] mixed-metal catalyst and a monometallic [Mo] counterpart. D,E) Detail of the temperature-resolved changes in the pre-edge XANES spectra features for the [MnMo] catalyst at the Mo-K (D) and Mn-K (E) absorption edge energies, respectively. Reaction conditions: $P = P_{atm}$, gas feed molar composition: $3NH_3$:$1H_2$:1CO.

indicating a shift in the average oxidation state of Mn ($OS_{Mn}$) from 1.3 to 1.8 (Figure 4B), that is, a slight oxidation rather than reduction for this metal. Additionally, intensification of the pre-edge feature indicated the evolution toward non-centrosymmetric Mn environments, such as distorted octahedral ($O_h$) coordination geometries (Figure 4E).

The above results prove a significant in situ nitridation of the oxidic catalyst precursor into a metal (oxy)nitride compound with cubic structure (*Fm-3m*) upon exposure to process conditions. Cubic MoN tends to stabilize a high density of nitrogen vacancies, leading to more stable $MoN_{1-x}$ structures, of which $\gamma$-$Mo_2N$ ($x$ = 0.5) is a commonly observed compound.[52–54] The experimental lattice parameter determined for the monometallic [Mo] material after exposure to catalysis conditions was consistent with a stoichiometry of $MoN_{0.46}$, confirming the development of a slightly N-defective $\gamma$-$Mo_2N$ as the working catalyst (Figure S12, Supporting Information).

To evaluate the impact of Mn doping on the thermodynamic and structural properties of *Fm-3m* Mo nitrides, periodic DFT calculations were performed using the PAW-RPBE-D3 level of theory (**Figure 5**). Figure 5C illustrates the predicted Gibbs free energy change ($\Delta G_f$) for nitride formation and the lattice parameter variation with Mn substitution into the primitive *c*-MoN lattice. For mixed MnMo nitrides, $\Delta G_f$ becomes increasingly negative with Mn content up to ≈50 at%, indicating greater stability over monometallic Mo nitride. Next, the thermodynamic properties of the corresponding oxo-nitride phases were analyzed by systematically replacing N atoms with O atoms at varying substitution levels in the optimized mono- and mixed-metal (Mo:Mn = 1:1 (*at*)) nitride structures. Figure 5D depicts the predicted evolution of $\Delta G_f$ for metal oxynitride structures as a function of nitrogen substitution by oxygen and the environmental oxygen chemical potential, referenced to $\mu^0_O$ at 0 K and $P_{O2}$ = 1 atm. The data indicate that mixed-metal oxynitride compounds are significantly more stable than their monometallic molybdenum-based counterparts, with $\Delta G_f$ turning negative at much lower oxygen chemical potentials. Furthermore, for a given oxygen chemical potential, $\Delta G_f$ is lower for the mixed-metal composition, suggesting enhanced stability. These findings imply that, under nitrifying reaction conditions, the retention of lattice oxygen from the oxidic catalyst precursor is thermodynamically more favorable for the [MnMo] mixed-metal catalyst than for its monometallic [Mo] counterpart.

The markedly asymmetric and broad diffraction signals registered experimentally in the XRD pattern for the fully developed [MnMo] catalyst (Figure S9, Supporting Information) hint at the presence of a comparatively high density of structural defects. Therefore, periodic DFT calculations were extended to further investigate the energetics of different types of point structural defects which are known to show feasible energetics in (oxy)nitride compounds of group VI-VII transition metals. Considering the bulk composition of the experimental catalyst (Mn:Mo = 1.1:1 (*at*)) and the exceptional stability predicted by DFT for the equimolar mixed-metal nitride, a $Mn_{0.5}Mo_{0.5}N(O)$ theoretical model compound was considered for these calculations (Figure S13, Supporting Information). The formation of nitrogen vacancies ($N_{vac}$) was predicted to be thermodynamically feasible, though less so compared to the monometallic *c*-MoN reference structure, even at notable defect densities of up to 25 %. However, the formation of cationic vacancies was predicted to incur energy penalties >0.3 eV defect$^{-1}$, even at comparatively low defect densities (≤10 %). Next, the formation of Schottky-type defects, through the concerted formation of cationic and anionic vacancies was studied. While this type of defects was found to be disfavored in a perfect nitride structure, defect formation energies progressively decreased with incorporation of

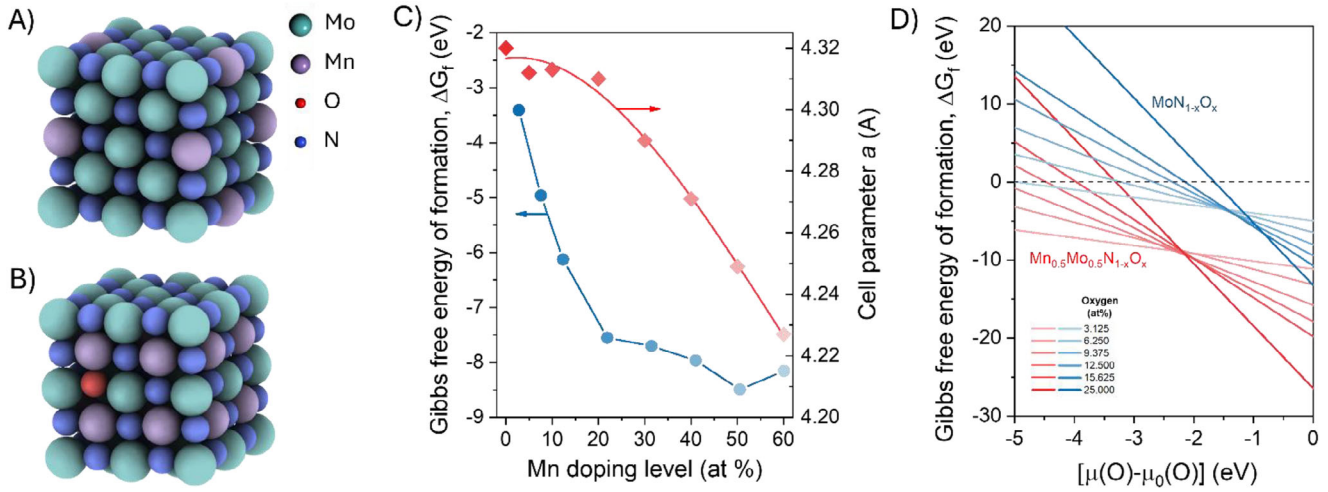


**Figure 5.** A,B) Schematic representation of 2×2×2 supercells for *Fm-3m* MoN additionally modified by isomorphic partial substitution of Mo by Mn (A) and of N by O (B). C) Evolution of the Gibbs free energy of formation and the lattice parameter (*a*) for *Fm-3m* MoMnN mixed-metal nitride as a function of the volumetric degree of Mo isomorphic substitution for Mn, as derived from periodic DFT calculations (PAW-RPBE-D3). D) Evolution of the Gibbs free energy of formation for monometallic and mixed-metal *Fm-3m* oxynitride materials as a function of the degree of lattice nitrogen substitution by oxygen (*at*%) and the environmental oxygen chemical potential, relative to that determined at 0 K and $P_{O2}$ = 1 atm reference conditions. Calculations have considered a nitrogen chemical potential $\mu_N$ corresponding to $P_{NH3}$ = 1.5 bar and $T$ = 723 K.

lattice oxygen in an oxynitride compound, particularly for the case of NN1 Schottky pairs involving $Mn_{vac}$ cationic defects. These results highlight that the retention of lattice oxygen under nitriding conditions, which is strongly favored in the [MnMo] mixed-metal catalyst, further contributes to the stabilization of lattice point defects in the crystal structure.

Complementing the theoretical predictions above, the short-range atomic order in the working [MnMo] catalyst was experimentally studied with Extended X-ray Absorption Fine Structure (EXAFS) spectroscopy. The monometallic [Mo] catalyst was also investigated under the same settings, for comparison purposes. **Figure 6** presents the $k^3$-weighted Fourier Transformed (FT-$\chi$(R)) functions in real space at the Mo-K and Mn-K absorption edges. These are shown for the oxidic catalyst precursors and after exposure to the reactive syngas/$NH_3$ atmosphere at progressively increasing temperatures, up to 873 K. The corresponding EXAFS spectra in the reciprocal $k^3$-space are given in Figure S14, Supporting Information. Examination of the temperature-resolved evolution of the Mo-K FT-EXAFS spectra for the reference [Mo] catalyst revealed a progressive elongation of the first-shell Mo-O(N) bond distance upon increasing reaction temperature, signifying a progressive nitridation (Figure 6A). In contrast, [MnMo] exhibited a comparatively abrupt upshift in bond distance at reaction temperatures between 723 and 773 K (Figure 6B). Following treatment under the nitriding atmosphere at 873 K, major differences in the direct coordination environment of Mo atoms were evident. As shown by the Continuous Cauchy Wavelet Transform (CCWT) of the EXAFS spectra, after exposure to reaction conditions, the monometallic [Mo] catalyst exhibited second-shell scattering signals closely matching those in bulk $\gamma$-$Mo_2N$ (Figure 6D). Conversely, [MnMo] lacked second-shell scattering contributions, indicating that Mn inhibited the formation of extended $MoN_x$ domains.

Analysis of the Mn-K FT-EXAFS revealed a progressive elongation of the first-shell Mn-(N,O) bond distance above 723 K, consistent with metal nitridation. Unlike the Mo-K edge evolution, a second-shell scattering contribution appeared in the range 2.1 <R(Å) <3.6 (no phase correction) and increased in amplitude with rising reaction temperature (Figure 6C). This additional signal, consistent with second-shell Mn-Mn scattering in a MnO (*Fm-3m*) reference compound, suggests the formation of Mn-enriched domains within the working catalyst, likely due to Mn segregation.

Based on the ab initio thermodynamic insights and X-ray diffraction results discussed above, various energetically plausible structural models (optimized using periodic DFT at the PAW-RPBE theory level) were considered to decode the complex structure of the [MnMo] catalyst via EXAFS fitting. A collection of cubic mixed Mn-Mo nitrides was considered as the basis for the first coordination shell analysis. In these models, Mn partially and isomorphically replaces Mo in the MoN structure (*Fm-3m*). The set of structural models included a stoichiometric $Mn_{0.5}Mo_{0.5}N$ nitride, but it additionally considered the presence of a variety of structural defects, that is, N (anionic) as well as Mn/Mo (cationic) vacancies, anti-site and NN1 Schottky pair defects (see Section 5 in the Supporting Information for supplementary details). Initially, fitting the experimental Mo-K and Mn-K EXAFS spectra was attempted using scattering paths extracted from the simulated structures, focusing on radial distances in the range of 1.0 <R(Å) <2.5 and 1.0 <R(Å) <2.1, that is, corresponding to the first coordination shell around Mo and Mn absorber atoms, respectively. However, some models failed to adequately describe the local structure of the working catalyst, either yielding physically implausible values for the free parameters or providing suboptimal fits to the experimental data. Among the structural models evaluated, a $Mn_{0.5}Mo_{0.5}N$ mixed-metal nitride with Schottky-type defects (involving $N_{vac}$ and $Mn_{vac}$ at a density of one defect per unit cell) provided the best match to the experimental spectrum at both Mn-K and Mo-K absorption edges. The analysis was then extended to radial (second shell) coordination distances

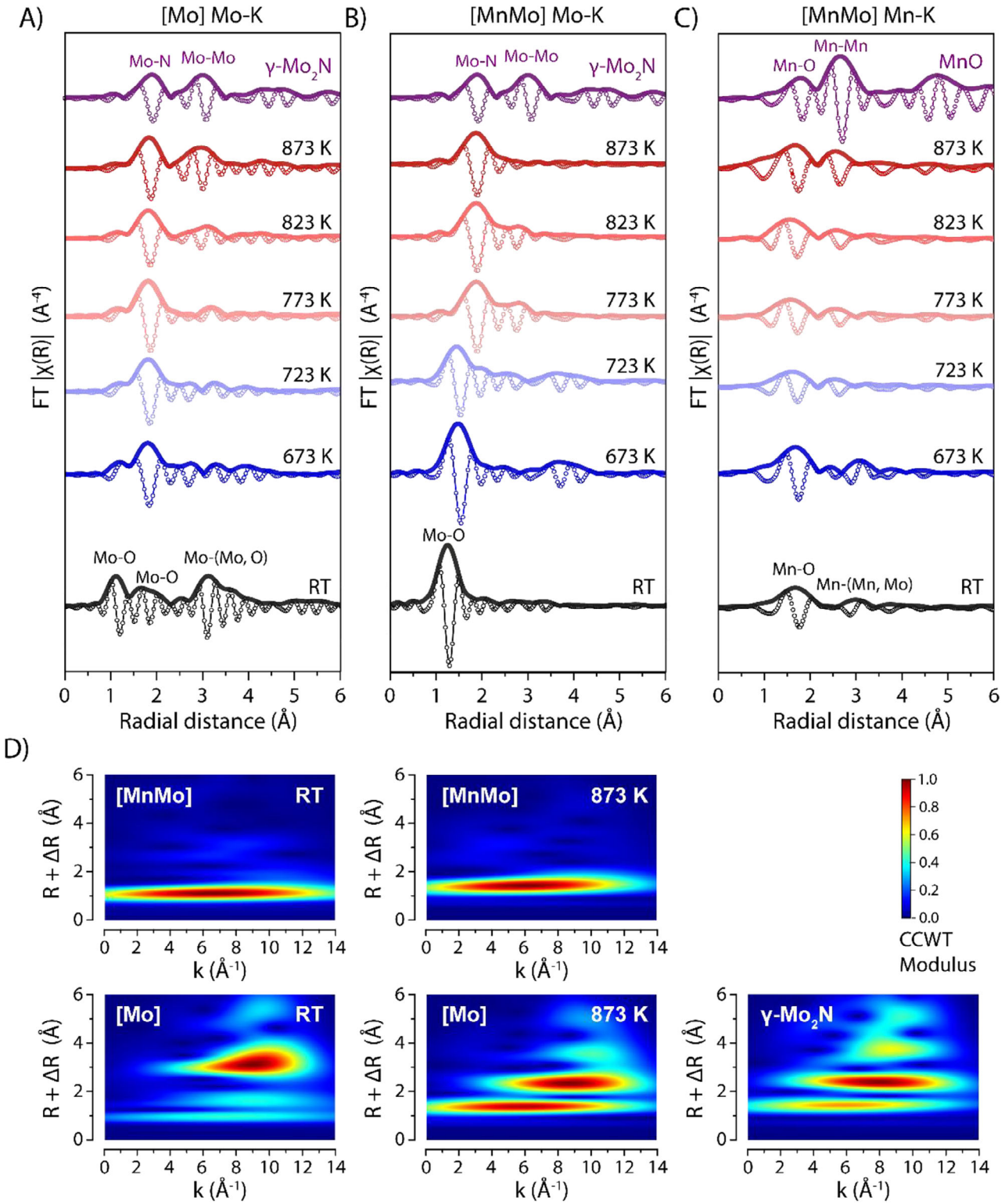


**Figure 6.** Fourier Transform FT-$\chi$(R) EXAFS functions in real space (no phase correction) collected at the A,B) Mo-K and C) Mn-K absorption edges, following exposure of the monometallic [Mo] (A), and the [MnMo] mixed-metal (B, C) catalyst precursors to reaction conditions ($3NH_3$:$1H_2$:1CO, $P_{atm}$) at increasing temperatures. The corresponding spectra for $\gamma$-$Mo_2N$ and MnO reference compounds are included for comparison purposes. D) Continuous Cauchy Wavelet Transforms (CCWT) of the $k^3$-weighted EXAFS functions for the [MnMo] (top) and [Mo] (bottom) catalyst (precursors) prior to, and after exposure to reaction conditions ($3NH_3$:$1H_2$:1CO, $P_{atm}$) at 873 K. The CCWT contour map for the $\gamma$-$Mo_2N$ reference compound is provided for comparison. The CCWT maps were calculated with a Cauchy order $n = 200$, and a Hanning apodization window applied in the $k$-range of 1–8/11 $Å^{-1}$, see Figure S14, Supporting Information for further details and the corresponding spectra in $k$-space.

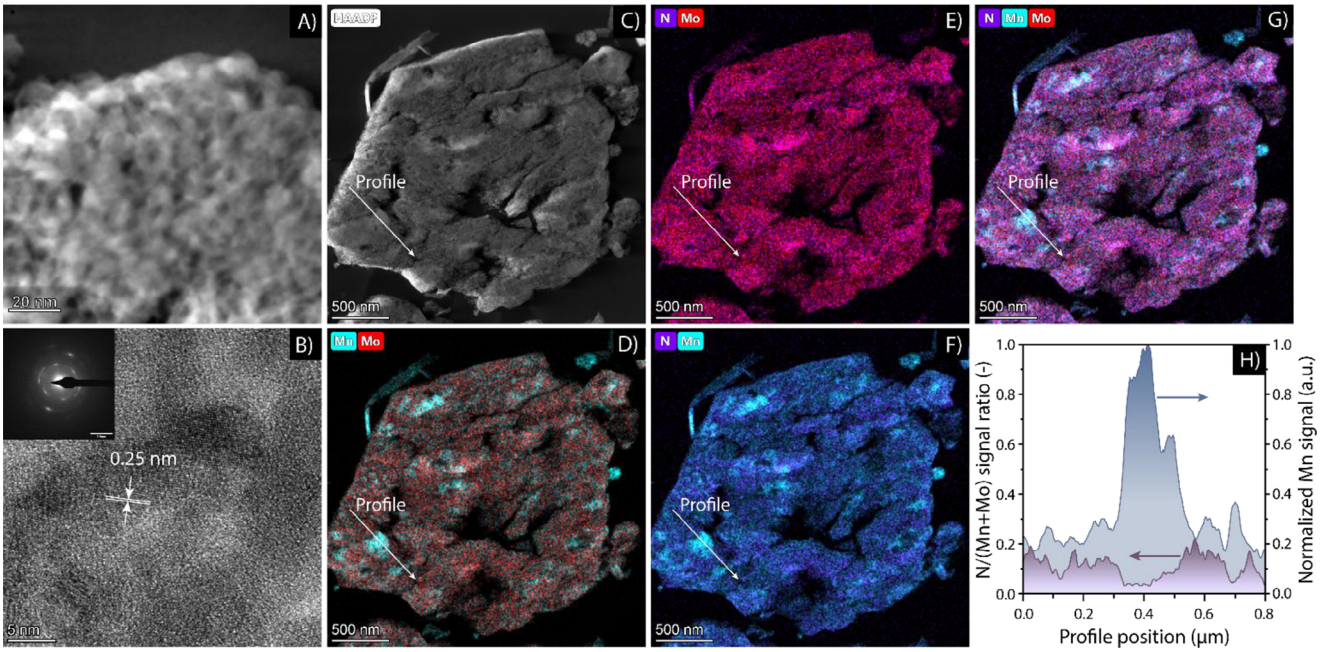


**Figure 7.** A,B) Representative high-resolution scanning transmission electron microscopy (HR-STEM) for the [MnMo] mixed-metal catalyst after exposure to reaction conditions for 600 min. The inset to panel (B) shows the corresponding Fast Fourier Transform (FFT) pattern. C) Representative high-angle annular dark-field (HAADF) STEM micrograph of a catalyst particle cross-section. Panels D–G) show the corresponding EDS elemental maps for Mn, Mo (D), N, Mo (E), N, Mn (F), and N, Mn, Mo (G), respectively. H) Spatial evolution of the local N/(Mn+Mo) EDS signal ratio, and normalized Mn signal, along the scanning profile marked on panels D–G. Reaction conditions: $T = 723$ K, $P = P_{atm}$, gas feed molar composition: $3NH_3$:1CO:$1H_2$.

in the range of 1.0 <R(Å) <3.6, where scattering events were observed in the Mn-K EXAFS spectrum. In this case, using solely the scattering paths simulated for the Schottky-defective MnMo mixed-metal nitride did not provide a satisfactory fit to the experimental data. Hence, the incorporation of additional scattering paths was attempted.

Building on the above first-principles thermochemistry predictions indicating increased oxophilicity due to Mn doping, along with Mn-enriched nanosized domains inferred from Mn-K EXAFS spectra, alternative coordination environments for Mn atoms in Mn-enriched cubic-symmetry clusters were explored. These included MnN, but also increasingly oxidic $MnN_xO_y$ oxynitride and MnO compounds. Particularly the inclusion of the second-shell scattering paths extracted from a $MnN_xO_y$ mixed-metal oxynitride cluster improved the overall fit significantly. However, achieving a satisfactory fit using the scattering paths extracted from the proposed models required high EXAFS Debye-Waller factors ($\sigma^2 > 0.01$ Å$^2$) and an increased number of variable parameters, pointing to a significant structural disorder in the developed [MnMo] catalyst. Taken together, the long-range XRD and short-range EXAFS structural analyses indicate the formation of a mixed-metal oxynitride as the active catalyst phase. Additionally, the analysis suggests the presence of local defects and compositional heterogeneities, likely in the form of Mn-enriched domains with lower local nitridation, which hinder a more detailed structural elucidation.

Nanospatial heterogeneities were further studied with high-resolution HAADF-STEM and EDS spectroscopy. As illustrated in **Figure** 7A,B, the comparatively large (>500 nm) crystals of the oxidic catalyst precursor transformed into individual, smaller (<20 nm) crystallites of the actual oxynitride catalyst under reaction conditions. The latter remained aggregated into larger structures which preserved the hexagonal aspect of the starting crystals in the oxidic precursor (Figure 7C), indicative of a pseudomorphic transformation into the working catalyst material under process conditions. Cross-sectional EDS compositional maps revealed a highly uniform distribution of Mo and Mn elements at both the nano- and mesoscales after 10 min of exposure to reaction conditions (Figure S15, Supporting Information), corresponding to a time-on-stream when the in situ catalyst formation was not yet complete. Following reaction for 600 min, that is, once the working catalyst had fully developed, the Mo spatial distribution remained uniform (Figure 7D–G). However, nanosized speckles enriched in Mn were observed throughout the material, confirming that a certain Mn segregation had taken place following the extensive nitridation of the catalyst. Moreover, the N/(Mo+Mn) atomic ratio was lower in these regions (Figure 7H), emphasizing locally lower nitridation extents. These nanoscale observations align well with results from complementary characterizations with broader sampling, which showed that the incorporation of Mn in the [MnMo] mixed-metal catalyst, compared to the [Mo] monometallic counterpart, inhibited N uptake and led to the formation of Mn-enriched domains which preserved a more oxidic nature under the strongly nitriding reaction conditions.

Finally, the molecular operation mode of the Mn promotional effect was investigated using periodic DFT modelling. Earlier computational mechanistic studies with unpromoted $\gamma$-$Mo_2N$ catalysts[47] showed HCN dissociation and further C—C coupling

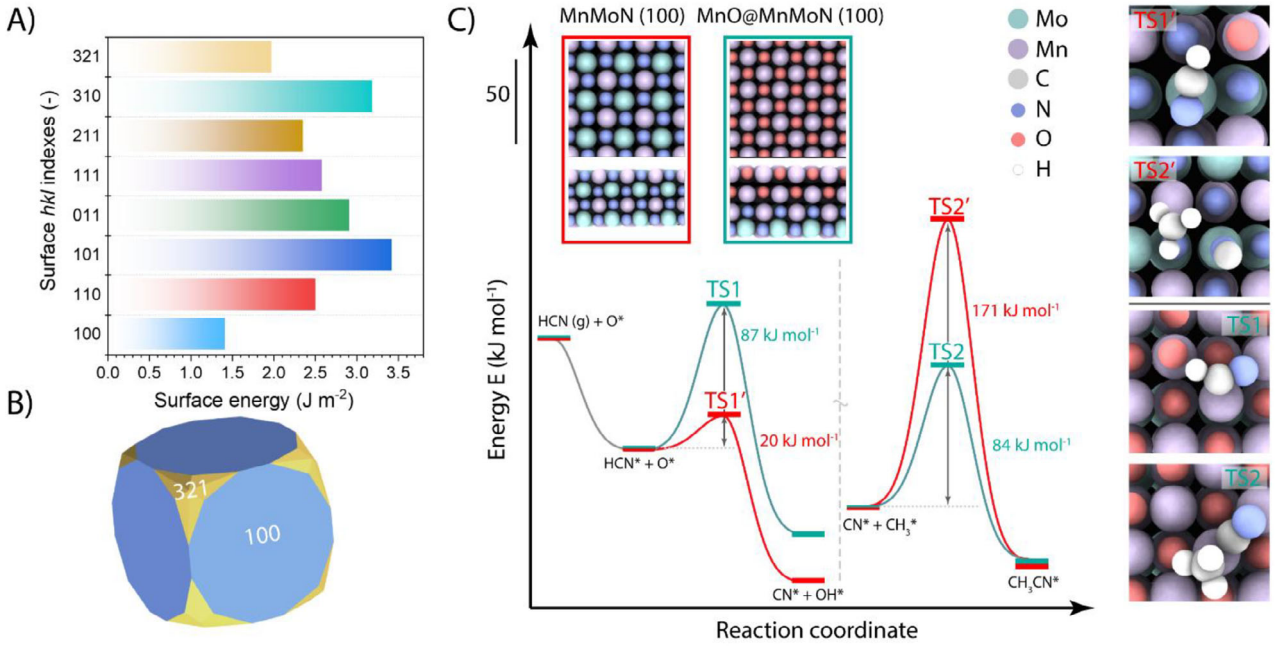


**Figure 8.** A) Surface energy, as determined by DFT calculations (PAW-RPBE-D3), for different facets of a MnMoN (*Fm-3m*) mixed-metal nitride. See Figure S16, Supporting Information for further details on the DFT-optimized surface models. B) Wulff construction for MnMoN crystallites. C) Calculated energy profile (PAW-RPBE-D3) for the adsorption of HCN and further oxygen-assisted hydrogen abstraction; as well as for further coupling of CN* and $CH_3$* adspecies on the MnMoN (100) nitride (profile in red) and MnO@MnMoN (100) oxynitride (turquoise) model surfaces. The inset to the plot provides zenithal and lateral views for the model catalyst surfaces considered. Zenithal views of the optimized structures for the corresponding transition states (TS) are depicted on the right-hand side from the plot.

reaction steps to be subjected to sizeable energy barriers (>120 kJ $mol^{-1}$) and thus likely to hold the highest degree of reaction rate control. Moreover, the central role of surface O* adspecies for dissociative HCN activation was elucidated. Thus, the present mechanistic study has focused on these reaction steps from HCN, a stable gas-phase intermediate product along the acetonitrile formation path.

Building on the battery of characterization results discussed earlier, the mixed-metal catalyst was modelled as a $Mn_{0.5}Mo_{0.5}N$ nitride with *Fm-3m* structure. As summarized in **Figure** 8A, the (100) surface exhibited the lowest surface energy, making it the dominant facet in the theoretical Wulff construction of mixed-metal nitride crystals (Figure 8B). Similar to the case of a $\gamma$-$Mo_2N$ monometallic catalyst, the (100) surface is thus expected to be predominantly exposed and was selected for building the MnMoN surface slab catalyst model. Additionally, to account for Mn-enriched, more oxidized regions in the catalyst, which have been experimentally inferred, a second surface model was considered. In this model, the top two atomic layers of the slab correspond to MnO, which also crystallizes in a cubic *Fm-3m* structure. This modified model is referred to as MnO@MnMoN.

Figure 8C shows the energy profiles calculated for HCN adsorption and O*-assisted dissociation, as well as for the subsequent direct coupling of CN* and $CH_3$* adspecies to acetonitrile on each surface model. On $Mn_{0.5}Mo_{0.5}N$, the energetically most stable adsorption configuration for HCN is oriented parallel to the surface, with both C and N atoms interacting with a single Mo atom ($E_{ads}$ = −69 kJ $mol^{-1}$). On MnO@MnMoN a parallel adsorption mode was also preferred, however, in this case di-sigma bonded, bridging two adjacent Mn atoms ($E_{ads}$ = −78 kJ $mol^{-1}$). From the most stable HCN binding configuration, H-abstraction by co-adsorbed O* proceeded with a lower barrier of 20.3 kJ $mol^{-1}$ on the fully nitridic surface than on MnO@MnMoN (87 kJ $mol^{-1}$). The resulting CN* species adopts preferentially a tilted atop configuration with the electron lone pair of the N atom interacting with a surface Mo atom in the case of MnMoN, whereas di-sigma binding to vicinal Mn atoms remains the preferred adsorption configuration in the case of the MnO@MnMoN surface oxynitride model.

Atop bonded CN* is predicted to entail a remarkably high energy barrier for C—C coupling to *$CH_3$ (171 kJ $mol^{-1}$). In stark contrast, di-sigma adsorption of CN* on MnO@$Mn_{0.5}Mo_{0.5}N$ enables further coupling with *$CH_3$ species to produce acetonitrile, with a notably lower barrier of 84 kJ $mol^{-1}$. This energy barrier is in fair agreement, within the accuracy of the DFT calculations, with the $E_{app}$ = 97 kJ $mol^{-1}$ determined experimentally for acetonitrile formation on the [MnMo] catalyst, and it is significantly lower than the $E_{app}$ = 151 kJ $mol^{-1}$ determined for the unpromoted, monometallic [Mo] counterpart, where extended molybdenum nitride domains are the dominant surface termination. Therefore, the results suggest that, while the C—C coupling reaction step is likely rate-determining on the extensively nitrided surface, it is significantly facilitated on more oxidic MnO-like (oxynitride) domains. Although a diverse range of surface motifs is expected on the real working [MnMo] catalyst, the reaction energetics predicted for these simplified surface models suggest that acetonitrile synthesis would proceed most efficiently at the

interface between mixed-metal nitride and Mn-rich oxynitride domains, where HCN dissociation and subsequent C—N coupling reactions are synergistically promoted.

Jointly, experimental and theoretical findings underscore the critical role of mixed-metal effects in tuning the extent of nitridation under the highly invasive syngas/ammonia reaction environment. The promotional effects observed in the unsupported [MnMo] catalyst result in a combination of selectivity and mass-specific time-yield to acetonitrile that surpasses those of previously reported bulk and supported materials (Table S5, Supporting Information).

## 3. Conclusions

Atomic-level metal mixing in a series of highly crystalline ammonium mixed-metal molybdate materials, featuring a common monoclinic *C 2/m* structure, provides an excellent platform to address mixed-metal synergisms in metal nitride catalysis for a direct synthesis of acetonitrile from syngas/ammonia mixtures. Among different 3d transition metals studied, Mn proves to be the most effective promoter, resulting in significantly enhanced performance compared to its single-metal counterparts. Monometallic [Mo] and [Mn] catalysts attained higher selectivities to HCN primary product (>49 %, carbon-basis within all organic products), while they proved less effective for further HCN activation and C—C coupling to acetonitrile (selectivity <32 %). In contrast, a [MnMo] mixed-metal material proved to be a superior catalyst, attaining a selectivity to acetonitrile >56 %, in combination with remarkable stability, resulting in a steady acetonitrile production rate of $5 \times 10^{-2}$ mmol $g^{-1}$ $min^{-1}$. Temperature-resolved X-ray diffraction (XRD), X-ray absorption spectroscopy (XAS), and depth-profiling X-ray photoelectron spectroscopy using synchrotron radiation (SR-XPS), revealed a swift nitridation of the oxidic catalyst precursor under reaction conditions, forming a cubic (*Fm-3m*) mixed-metal oxynitride phase as the working catalyst. This transformation aligns with first-principles thermochemistry predictions of a significant stabilization of oxynitride compounds, induced by Mn doping. As ascertained with complementary long- and short-range structural analyses (XRD, EXAFS), the incorporation of Mn disrupts the formation of extended $MoN_x$ domains under the strongly nitriding process conditions. This is supported by direct nanoscale EDS compositional mapping, which proves the stabilization of Mn-enriched regions within the working mixed-metal catalyst, that exhibit a lower local nitridation degree and thus retain a more oxidic character. Reaction modeling with periodic DFT suggests that these Mn-rich oxidic domains enhance the conversion of the stable HCN primary product by facilitating C—C coupling compared to fully nitrided surfaces, thereby promoting acetonitrile production. The results emphasize the significance of mixed-metal effects to adjust the material's nitridation extent under the aggressive syngas/ammonia reaction atmosphere, resulting in catalysis promotional effects for the direct synthesis of acetonitrile from sustainable $C_1$ and $N_1$ resources.

## 4. Experimental Section

*Material Synthesis*: A series of crystalline ammonium M (II) molybdate materials (M = Zn, Cu, Ni, Co or Mn) were synthesized via a co-precipitation route[55,56] and applied as catalyst precursors. A $(NH_4)_6Mo_7O_{24}\cdot 4H_2O$ aqueous solution (0.04 M, ≥ 99.3 %, Merck) was prepared, and its pH was adjusted to 9.8 by addition of an ammonium hydroxide aqueous solution (25 vol%). 100 mL of this solution were magnetically stirred and heated to 363 K in an oil bath. Next, 15 ml of a 1.4 M aqueous solution of the corresponding metal nitrate precursor for the divalent 3d transition metal M ($Zn(NO_3)_2.6H_2O$, ≥99 % Sigma-Aldrich; $Cu(NO_3)_2.2.5H_2O$, ≥98 % Alfa Aesar; $Ni(NO_3)_2.6H_2O$, 99.999 % Sigma-Aldrich; $Co(NO_3)_2.6H_2O$, ≥98 % ACROSS organics; or $Mn(NO_3)_2.4H_2O$, 99.999 % Merck) were added drop-wise on the molybdate solution at a constant rate of 0.5 mL $min^{-1}$ at 363 K. The precipitate was aged in the liquors for 30 min at the same temperature, isolated by filtration, washed extensively with boiling water, and dried in an oven at 373 K overnight. The crystalline ammonium M (II) molybdate materials series were labeled as [MMo], (M = Zn, Cu, Ni, Co or Mn). $MoO_3$ (>99.5 %, Merck) and $MnO_2$ (99.9 %, NanoShel) nanopowders were applied as precursors for comparative monometallic catalysts and referred to as [Mn] and [Mo], respectively. $\gamma$-$Mo_2N$ standard material was synthesized from $MoO_3$ nanopowder by nitridation treatment at 973 K for 5 h (5 K $min^{-1}$) under flow of 40 vol% $N_2$ in $H_2$ in a packed-bed quartz reactor.

*Characterization Methods—Compositional Analysis*: Bulk catalyst compositions were determined, at various activation and usage stages, by inductively coupled plasma optical-emission spectrometry (ICP-OES) in a ThermoScientific, iCAP PRO spectrometer. Samples were disaggregated in aqua regia (3:1 v/v $HCl/HNO_3$) under inert Ar atmosphere, in a gloves bag. Carbon and nitrogen contents were determined in a Eurovector, EuroEA 3000 CHNS analyzer using sulfanilamide as standard.

*Powder X-Ray Diffraction*: The crystalline structure of the ammonium M (II) molybdate materials series (M = Zn, Cu, Ni or Co) was studied by high-resolution powder X-ray diffraction (HRXRD) using monochromatic synchrotron radiation. Diffractograms were collected at the BL16-NOTOS beamline of the ALBA synchrotron (Cerdanyola del Vallès, Spain). The [MoM] precursors (M = Zn, Cu, Ni or Co) were transferred into glass capillaries (outer diameter 0.5 mm, wall thickness 0.01 mm) and diffractograms collected d in a Debye-Scherrer geometry at 19.5 keV photon energy ($\lambda$ = 0.6359 Å refined using NIST 640e standard) applying a MYTHEN position sensitive detector[57] in the $2\theta$ range of 3–60 degrees.

The structural evolution of the [MoMn] catalyst precursor under varying temperatures and reaction times in the syngas/$NH_3$ mixture was also studied using powder X-ray diffraction. Diffractograms were recorded in Bragg-Brentano geometry using a PANalytical CUBIX diffractometer (Cu K$\alpha$ radiation, $\lambda_1$ = 1.5406 Å, $\lambda_2$ = 1.5444 Å, $I_2/I_1 = 0.5$, goniometer radius 200 mm) equipped with a X'Celerator detector. For each measurement, non-air-sensitive samples were finely grounded and filled in a stainless-steel round sample holder. Once mounted on the diffractometer, holders were spun at 20 rpm and the measurement performed with a fixed divergence slit (1/8° aperture) from 3.5 to 90.0 degree ($2\theta$), using scanning steps and accumulation time per step of 0.020° $step^{-1}$ ($2\theta$) and 35 s $step^{-1}$, respectively. Following exposure to activation/reaction conditions, air-sensitive samples were handled in a nitrogen-filled glove box ($O_2$ < 1 ppm, $H_2O$ < 1 ppm) and mounted on an air-tight Si (911) plate holder sealed with Kapton. In this case, measurements were performed with a variable divergence slit irradiating a 3 mm x 10 mm (length x width) sample area, using 0.020° $step^{-1}$ ($2\theta$), 17 s $step^{-1}$ step sizes and scanning speed, respectively. Selected materials originating from the exposure of the [MoMn] precursor to reaction conditions at different temperatures and times were further investigated by high-resolution X-ray diffraction at the BL04-MSPD beamline of the ALBA synchrotron.[58] Powder samples were loaded into glass capillaries (outer diameter 0.5 mm, wall thickness 0.01 mm) in a glove box under protective $N_2$ atmosphere ($O_2$ < 1 ppm, $H_2O$ < 1 ppm). The capillaries were sealed with clay in the glove box and finally flame-sealed outside. Measurements were performed in Debye-Scherrer geometry at 30 keV photon energy ($\lambda$ = 0.4125 Å refined using NIST 640e standard) using a MYTHEN position sensitive detector[57] in the $2\theta$ range of 2–120 degrees. Four diffraction patterns (45 min $scan^{-1}$) were collected for each sample and averaged to improve signal/noise ratio. Additionally, $\gamma$-$Mo_2N$ was measured as a reference material.

*Electron Microscopy*: Field emission scanning electron microscopy (FE-SEM) experiments were performed in a FE-SEM ZEISS ULTRA 55 microscope to assess crystal size and morphology. As-synthesized catalyst precursor materials were finely grounded and deposited on a double-adhesive-face conductive carbon-tab stuck on the SEM sample holder and imaged without any additional sputter coating. High-resolution transmission electron microscopy (HR-TEM) and high-angle annular dark-field scanning-transmission electron microscopy (HAADF-STEM) experiments were carried out in a FEI TITAN G2 microscope equipped with a Schottky-type field-emission gun and operated at an acceleration voltage of 300 kV. Prior to observation, samples exposed to activation/reaction conditions were embedded in a low-viscosity epoxy resin (Spurr) under exclusion of air. Then, slices of the embedded material were produced, with nominal thickness of 250 nm, on a Reichert Ultracut ultramicrotome mounting a Diatome diamond knife and deposited onto Cu TEM grids (150 mesh) coated with a continuous formvar film. Cross-sectional compositional maps were generated from the ultramicrotomed specimens by means of a Super X quadruple energy-dispersive spectroscopy (EDS) detector with automated drift correction.

*X-Ray Photoelectron Spectroscopy*: X-ray photoelectron spectra were collected in a SPECS spectrometer equipped with a Phoibos 150 MCD-9 detector, using a non-monochromatic (AlK$\alpha$ = 1486.6 eV) X-ray source, an analyzer pass energy of 30 eV, and an X-ray power of 100 W under an operating pressure of $10^{-4}$ mPa. Following exposure to activation/reaction conditions in a quartz tubular reactor, samples were transferred to a $N_2$-filled glove box (<1 ppm $O_2$, <1 ppm $H_2O$) under exclusion of air, mounted onto double copper film-stainless steel holders and then transferred to the UHV line connected to the spectrometer in an air-tight transfer suitcase under nitrogen atmosphere.

For selected samples, near-surface depth-profiling compositional investigations were performed with synchrotron radiation XPS (SR-XPS) at the Near-Ambient Pressure XPS, NAPP branch of CIRCE beamline of the ALBA Synchrotron Light Source, Barcelona (Spain), an undulator beamline wherein a plane mirror and three diffraction gratings are used to cover the source energy range from 100 to 2000 eV. Data acquisition was performed using a PHOIBOS 150NAP electron energy analyzer (SPECS). Spectra were acquired with an exit slit of 60 µm and a pass energy of 20 eV irradiating a spot on the powder samples mounted onto copper film-stainless steel holders and transferred from a glove box to the UHV line of the end-station under exclusion of air. Incident photon energies of 400, 500, 600 and 750 eV were applied to record Mo3d, Mn3p, N1s/Mo3p, and C1s core-levels with variable photoelectron escape depths, as determined with electron inelastic mean free paths predicted by the Tanuma-Powell-Penn formalism (TTP2M).[59] The XPS data were analyzed using CASA XPS Software and applying Shirley-type spectral backgrounds and Gaussian/Lorentzian curves for spectra fitting. Binding energies were calibrated to the C1s signal for adventitious carbon at 284.6 eV.

*X-Ray Absorption Spectroscopy*: X-ray absorption spectra were recorded at the Mo-K (19.9995 keV) and Mn-K (6.539 keV) absorption edges at the BL22-CLÆSS[60] beamline station of the ALBA synchrotron light source, Barcelona (Spain). The beam was monochromatized using a (311) double crystal monochromator, and harmonic rejection was performed using Pt-coated silicon mirrors. Samples and air-sensitive standards were ground, diluted in boron nitride (to circumvent self-absorption effects) and mounted in air-tight holders sealed with Kapton film in an Ar-filled glove box ($O_2$ < 1 ppm, $H_2O$ < 1 ppm). Measurements were performed at room temperature in fluorescence mode using a fluorescence solid Silicon Drift detector. Reference metal oxide materials were prepared the same way, shaped into pellets (Ø = 13.2 mm) and measured in transmission mode employing ion chambers filled with appropriate gases in order to absorb 15 % and 80 % in the $I_0$ and $I_1$, respectively. At least 3 scans were recorded to ensure spectral reproducibility and appropriate signal-to-noise ratio. Data treatment has been carried out using Athena for $\chi$(k) function extraction and Artemis (Demeter software package)[61] for EXAFS data analysis.

*Catalysis Testing*: Catalysis tests were performed in an XS15-Microactivity reactor (Micromeritics). Pure $NH_3$ (Linde, 99.9 %), a synthetic syngas mixture (45 % CO, 45 % $H_2$, 10 % Ar (vol), Linde) and $H_2$ (Linde, 99.9999 %) were fed from gas cylinders through mass-flow controllers (MFCs, Bronkhorst) into a 316L stainless steel tubular reactor inserted axially in a furnace. The synthetic syngas stream was purified in a high-pressure filter, filled with activated carbon pellets (Ø = 3 mm), located upstream of the corresponding MFC, in order to retain any volatile metal carbonyl compounds which may be entrained from the gas cylinder. The particles of the catalyst precursor (60–1260 mg, Ø = 200–400 µm) were diluted with SiC granules (Ø = 600–800 µm) to improve the overall heat conductivity and packed in a fixed-bed with a total volume of 1.4 $cm^3$. The tubular reactor is equipped with a chemically inert quartz in-liner (I.D. = 7 mm) and a sapphire sheath hosting a type-K SS316-coated thermocouple (O.D. = 2.9 mm), inserted axially to provide the temperature reading at the center of the catalyst bed. Temperature was controlled in the range of 673–873 K by means of a PID controller, while pressure was controlled (1.2–3 bar) by a servocontrolled micrometering valve located downstream of the reactor. The flow of the feed stream to the reactor was adjusted (15–50 mL $min^{-1}$) to attain different, preset gas space velocities. The product stream leaving the reactor was depressurized and directed to a SCION gas chromatograph (GC) equipped with FID and TCD detectors. To assess the evolution of performance metrics as a function of the gas-solid contact time, one set of experiments was performed at T = 723 K, P = 3 bar, and varying reactant weight hourly space velocities (WHSV), with a single catalyst load. Following catalyst in situ activation, the highest WHSV (shortest reactant-solid contact time) of 35 $h^{-1}$ was kept for 4 h until pseudo-steady state was reached. Then progressively lower WHSV were tested stepwise, down to 1.2 $h^{-1}$, with dwell times of 3–4 h to attain a pseudo-steady state at each condition. Initial reaction transients were studied in the same setup, monitoring the composition of the outlet stream by means of mass spectrometry in an OmniStar GSD320 mass spectrometer (Pfeiffer) equipped with C-SEM and Faraday detectors and connected online. All transfer lines to the GC (or alternatively to the MS) were heat traced to 453 K to prevent product condensation as well as deposition of $(NH_4)_2CO_3$ or urea, which may form by reaction of $NH_3$ and $CO_2$ (side-product of the syngas conversion reaction).

*Density Functional Theory and Ab Initio Thermochemistry*: Periodic Density Function Theory (DFT) calculations were performed using QE code suite in version 7.2[62,63] interfaced to Atomic Simulation Environment (ASE) and Advanced Nanolabo scripting environments. Calculations have been carried out adopting the generalized gradient approximation (GGA) with the revised Perdew-Burke-Ernzerhof (RPBE) density functional.[64] The semi-empirical method of Grimme-D3 was employed to describe long-range dispersion interactions. The interaction between valence and core electrons was described using the Projected Augmented Wave method (PAW).[65] A plane-wave basis set was used with a cut-off energy of 650 eV. Fractional occupancies were calculated using a Gaussian smearing function with a width of 0.10 eV. All calculations were performed considering spin polarization. A Broyden-Fletcher-Goldfarb-Shanno algorithm was applied for geometry optimizations with an interatomic force threshold of $2.5 \cdot 10^{-2}$ eV $Å^{-1}$. Monkhorst-Pack grids were used to approximate the value of an integral over the Brillouin zone with 6 × 6 × 6 k-point meshes to sample the reciprocal space for 2×2×2 supercells. All atoms were allowed to relax when optimizing cubic supercells. Gas-phase molecules were optimized in a $10^3$ $Å^3$ cubic vacuum box and reciprocal space sampling was applied to the gamma point. A 4 × 4 × 1 k-point mesh was used to sample the reciprocal space for slabs. The latter were constructed in 2×2 cells with four atomic layers and spaced by a perpendicular vacuum size greater than 15 Å to avoid spurious interactions with periodic replicas. The two top atomic layers, and all atoms for adsorbate molecules, were allowed to relax fully during geometry optimization, while the two layers at the bottom of the metal slab were kept frozen to emulate bulk effects. Reaction transition states were identified using the climbing image nudged elastic band (CI-NEB) method.[66] Additional details on the calculations are provided in the Supporting Information.

*Statistical Analysis*: Catalytic performance metrics are reported as averages from independent experimental tests. Each independent test included fresh catalyst loading, activation, and performance evaluation, all

conducted starting from a single large batch of the catalyst precursor material. Experimental uncertainties are expressed in all cases as the standard error of the mean (SEM). The exact number of replicates (n) for each experiment is provided in the corresponding figure captions. The EXAFS data were analyzed using the Artemis module of the Demeter software suite (v0.9.26). The uncertainty (standard error) for each free parameter was estimated through the correlation-aware error analysis built into Artemis, which utilizes the covariance matrix resulting from the least-squares fitting routine. These values represent statistical uncertainties, assuming the fitting model is adequate and residuals are random. Fit quality was further evaluated using the R-factor (a measure of deviation between data and model) and a reduced $\chi_\nu^2$ parameter, both of which are reported in the EXAFS fitting results included in the ESI. The number of independent points ($N_{ind}$) was calculated using the Nyquist criterion. Parameter values that significantly degraded the fit quality or yielded nonphysical values (e.g., negative $\sigma^2$ or unreasonably large $\Delta R$) were flagged and led to the exclusion of the corresponding structural model from further consideration.

## Supporting Information

Supporting Information is available from the Wiley Online Library or from the author.

## Acknowledgements

This work received funding from the European Research Council (ERC-2019-CoG 864195). Additionally, parts of this study were funded through the projects PID2022-140111OB-I00, and CEX2021-001230-S, funded by MCIN/AEI/10.13039/501100011033/ and "ERDF A way of making Europe," as well as part of the Advanced Materials program and was supported by MCIN with funding from the European Union Next Generation EU (PRTR-C17.I1) and by Generalitat Valenciana (project MAF/2022/012). High-resolution XRD, SR-XPS and XAS experiments were performed at the BL04-MSPD, BL24-CIRCE and BL22-CLÆSS and BL16-NOTOS beamlines at ALBA Synchrotron with the collaboration of ALBA staff. M.D. W.H. acknowledges the predoctoral grant PRE2019-087571, funded by the Spanish Ministry of Science and Innovation MCIN/AEI/10.13039/501100011033/ and "ERDF A way of making Europe." T.R. acknowledges support by the Ramón y Cajal Program (Grant No. RYC2022-037355-I), funded by MCIN/AEI/10.13039/501100011033 and by the European Union NextGenerationEU/PRTR. M. A. Herrero, J. Soriano and M.D. Soriano (ITQ) and M. M. Abad (UG) are acknowledged for experimental contributions to elemental analysis, (SR)XPS and EDS experiments, respectively. The electron microscopy unit at UPV is acknowledged for support with, and maintenance of, their electron microscopy facilities.

## Conflict of Interest

The authors declare no conflict of interest.

## Author Contributions

M.E.M.-M.: Conceptualization; Investigation; Methodology; Formal analysis; Data curation; Writing – original draft; and Writing – review & editing. W.H.: Investigation; Methodology; Formal analysis; Data curation; Writing – original draft. T.R.: Investigation; Methodology; Formal analysis; Data curation; Writing – original draft. P.C.: Investigation; Methodology; Formal analysis. V.P.D.: Investigation; Methodology; Formal analysis. A.M.: Investigation; Methodology; Formal analysis. G.A.: Investigation; Methodology; Formal analysis. G.P.: Conceptualization; Methodology; Formal analysis; Funding acquisition; Project administration; Supervision; Writing – original draft; and Writing – review & editing.

## Data Availability Statement

The data that support the findings of this study are available from the corresponding author upon reasonable request.

## Keywords

Bimetallic catalysts, first-principles thermochemistry, in situ spectroscopy, mixed-metal catalysts, nitrile synthesis, sustainable chemistry, transition metal nitrides

Received: April 12, 2025
Revised: August 13, 2025
Published online:

[1] J. Xie, Y. Xie, *Chem. Eur. J.* **2016**, *22*, 3588.
[2] F. Chang, W. Gao, J. Guo, P. Chen, *Adv. Mater.* **2021**, *33*, 2005721.
[3] Z. Cheng, W. Qi, C. H. Pang, T. Thomas, T. Wu, S. Liu, M. Yang, *Adv. Funct. Mater.* **2021**, *31*, 2100553.
[4] S. Wang, F. Gong, Q. Zhou, Y. Xie, H. Li, M. Li, E. Fu, P. Yang, Y. Jing, R. Xiao, *Appl. Catal. B* **2023**, *339*, 123134.
[5] H. Hu, X. Wang, Z. Zhang, J. Liu, X. Yan, X. Wang, J. Wang, J. P. Attfield, M. Yang, *Adv. Mater.* **2025**, *37*, 2415421.
[6] Q. Luo, C. Lu, L. Liu, M. Zhu, *Green Energy Environ.* **2023**, *8*, 406.
[7] L. Verger, C. Xu, V. Natu, H.-M. Cheng, W. Ren, M. W. Barsoum, *Curr. Opin. Solid State Mater. Sci* **2019**, *23*, 149.
[8] Y. Bao, H. Zou, S. Du, X. Xin, S. Wang, G. Shao, F. Zhang, *Adv. Mater.* **2023**, *35*, 2302276.
[9] A.-M. Alexander, J. S. J. Hargreaves, *Chem. Soc. Rev.* **2010**, *39*, 4388.
[10] R. Jamil, R. Ali, S. Loomba, J. Xian, M. Yousaf, K. Khan, B. Shabbir, C. F. McConville, A. Mahmood, N. Mahmood, *Chem. Catal.* **2021**, *1*, 802.
[11] R. Zeng, Y. Yang, X. Feng, H. Li, L. M. Gibbs, F. J. DiSalvo, H. D. Abruña, *Sci. Adv.* **2025**, *8*, abj1584.
[12] W. N. Porter, K. K. Turaczy, M. Yu, H. Mou, J. G. Chen, *Chem. Sci.* **2024**, *15*, 6622.
[13] M. Abdelgaid, S. Perera, R. Ahmadov, M. D. Porosoff, G. Mpourmpakis, *Chem. Eng. J.* **2025**, *510*, 161774.
[14] Q. Cao, W. Sun, Z. Xiao, X. Zhou, L. Lu, H. Hou, Y. Chen, L. Wang, *Small* **2024**, *20*, 2404202.
[15] S. Tada, M. Terashima, D. Shimizu, N. Asakuma, S. Honda, R. Kumar, S. Bernard, Y. Iwamoto, *Angew. Chem., Int. Ed.* **2024**, *63*, 202410961.
[16] S. T. Oyama, M. Boudart, *J. Res. Inst. Catal., Hokkaido Univ.* **1980**, *28*, 305.
[17] S. Ted Oyama, *J. Solid State Chem.* **1992**, *96*, 442.
[18] A. Garg, M. Milina, M. Ball, D. Zanchet, S. T. Hunt, J. A. Dumesic, Y. Román-Leshkov, *Angew. Chem., Int. Ed.* **2017**, *56*, 8828.
[19] L. Volpe, M. Boudart, *J. Phys. Chem.* **1986**, *90*, 4874.
[20] W. Zheng, T. P. Cotter, P. Kaghazchi, T. Jacob, B. Frank, K. Schlichte, W. Zhang, D. S. Su, F. Schüth, R. Schlögl, *J. Am. Chem. Soc.* **2013**, *135*, 3458.
[21] X. Fan, H. Zhang, J. Li, Z. Zhao, C. Xu, J. Liu, A. Duan, G. Jiang, Y. Wei, *Chin. J. Catal.* **2014**, *35*, 286.
[22] S. M. Hunter, D. H. Gregory, J. S. J. Hargreaves, M. Richard, D. Duprez, N. Bion, *ACS Catal.* **2013**, *3*, 1719.
[23] R. Michalsky, A. M. Avram, B. A. Peterson, P. H. Pfromm, A. A. Peterson, *Chem. Sci.* **2015**, *6*, 3965.
[24] G. A. Olah, G. K. S. Prakash, A. Goeppert, *J. Am. Chem. Soc.* **2011**, *133*, 12881.
[25] J. G. Chen, R. M. Crooks, L. C. Seefeldt, K. L. Bren, R. M. Bullock, M. Y. Darensbourg, P. L. Holland, B. Hoffman, M. J. Janik, A. K. Jones,

M. G. Kanatzidis, P. King, K. M. Lancaster, S. v. Lymar, P. Pfromm, W. F. Schneider, R. R. Schrock, *Science (1979)* **2018**, *360*, aar6611.
[26] A. Martin, V. N. Kalevaru, *ChemCatChem* **2010**, *2*, 1504.
[27] A. J. Hubert, E. Puentes, in *Catalysis in C1 Chemistry*, (Ed.: W. Keim), Springer Netherlands, Dordrecht, **1983**, pp. 219-244.
[28] G. Chen, T. Liang, P. Yoo, S. Fadaeerayeni, E. Sarnello, T. Li, P. Liao, Y. Xiang, *ACS Catal.* **2021**, *11*, 7987.
[29] S. R. Foit, I. C. Vinke, L. G. J. de Haart, R.-A. Eichel, *Angew. Chem., Int. Ed.* **2017**, *56*, 5402.
[30] R. Zhao, H. Xie, L. Chang, X. Zhang, X. Zhu, X. Tong, T. Wang, Y. Luo, P. Wei, Z. Wang, X. Sun, *EnergyChem* **2019**, *1*, 100011.
[31] K. Nozaki, E. Cerrito, US3410904, **1968**.
[32] D. R. Corbin, S. Schwarz, G. C. Sonnichsen, *Catal. Today* **1997**, *37*, 71.
[33] R. Walter, US2821537A, **1952**.
[34] G. A. Kliger, L. S. Glebov, T. P. Popova, E. v. Marchevskaya, V. G. Beryezkin, S. M. Loktev, *J. Catal.* **1988**, *111*, 418.
[35] H. Kölbel, J. Trapper, *Angew. Chem., Int. Ed. Engl.* **1966**, *5*, 843.
[36] T. Sango, N. Fischer, R. Henkel, F. Roessner, E. van Steen, M. Claeys, *Appl. Catal., A* **2015**, *502*, 150.
[37] N. Fischer, R. Henkel, H. Kotzé, M. Fürst, J. Olivier, J. Neethling, M. Claeys, *Catal. Commun.* **2016**, *87*, 14.
[38] G. Olive, S. Olive, US4179462, **1978**.
[39] H. Hamada, Y. Kuwahara, Y. Matsuno, K. Wakabayashi, *J. Jpn. Pet. Inst.* **1987**, *30*, 188.
[40] K. N. Kim, A. M. Lane, *J. Catal.* **1992**, *137*, 127.
[41] A. A. Hummel, M. V. Badani, K. E. Hummel, W. N. Delgass, *J. Catal.* **1993**, *139*, 392.
[42] R. B. Anderson, J. F. Shultz, B. Seligman, W. K. Hall, H. H. Storch, *J. Am. Chem. Soc.* **1950**, *72*, 3502.
[43] J. F. Shultz, W. K. Hall, B. Seligman, R. B. Anderson, *J. Am. Chem. Soc.* **1955**, *77*, 213.
[44] N. E. Thornburg, A. B. Thompson, J. M. Notestein, *ACS Catal.* **2015**, *5*, 5077.
[45] J. A. Schaidle, L. T. Thompson, *J. Catal.* **2015**, *329*, 325.
[46] H. Schulz, *Catal. Today* **2014**, *228*, 113.
[47] A. C. Kizilkaya, M. E. Martínez-Monje, G. Prieto, *Catal. Today* **2024**, *442*, 114947.
[48] T. Tatsumi, S. Kunitomi, J. Yoshiwara, A. Muramatsu, H. Tominaga, *Catal. Lett.* **1989**, *3*, 223.
[49] Y. L. Leung, P. C. Wong, K. A. R. Mitchell, K. J. Smith, *Appl. Surf. Sci.* **1998**, *136*, 147.
[50] X. Yan, T. Xu, G. Chen, S. Yang, H. Liu, Q. Xue, *J Phys D Appl Phys* **2004**, *37*, 907.
[51] T. R. Gengenbach, G. H. Major, M. R. Linford, C. D. Easton, *J. Vac. Sci. Technol., A* **2021**, *39*, 013204.
[52] Z. N. Jaf, H. A. Miran, Z.-T. Jiang, M. Altarawneh, *Rev. Chem. Eng.* **2023**, *39*, 329.
[53] E. A. Goldfine, J. K. Wenderott, M. E. Sweers, S. Pandey, L. C. Seitz, M. J. Bedzyk, S. M. Haile, *Inorg. Chem.* **2022**, *61*, 16760.
[54] C. Zhang, E. A. Goldfine, K. He, J. K. Wenderott, S. A. Pandey, R. dos Reis, J. Shen, C. Wolverton, M. J. Bedzyk, K. R. Poeppelmeier, V. P. Dravid, S. M. Haile, *Chem. Mater.* **2024**, *36*, 1123.
[55] G. Prieto, S. Beijer, M. L. Smith, M. He, Y. Au, Z. Wang, D. A. Bruce, K. P. de Jong, J. J. Spivey, P. E. de Jongh, *Angew. Chem., Int. Ed.* **2014**, *53*, 6397.
[56] D. Levin, S. L. Soled, J. Y. Ying, *Inorg. Chem.* **1996**, *35*, 4191.
[57] A. Bergamaschi, A. Cervellino, R. Dinapoli, F. Gozzo, B. Henrich, I. Johnson, P. Kraft, A. Mozzanica, B. Schmitt, X. Shi, *J. Synchrotron Radiat.* **2010**, *17*, 653.
[58] F. Fauth, R. Boer, F. Gil-Ortiz, C. Popescu, O. Vallcorba, I. Peral, D. Fullà, J. Benach, J. Juanhuix, *Eur. Phys. J. Plus* **2015**, *130*, 160.
[59] S. Tanuma, C. J. Powell, D. R. Penn, *Surf. Interface Anal.* **1993**, *20*, 77.
[60] L. Simonelli, C. Marini, W. Olszewski, M. Ávila Pérez, N. Ramanan, G. Guilera, V. Cuartero, K. Klementiev, *Cogent Phys.* **2016**, *3*, 1231987.
[61] B. Ravel, M. Newville, *J. Synchrotron Radiat.* **2005**, *12*, 537.
[62] P. Giannozzi, S. Baroni, N. Bonini, M. Calandra, R. Car, C. Cavazzoni, D. Ceresoli, G. L. Chiarotti, M. Cococcioni, I. Dabo, A. Dal Corso, S. de Gironcoli, S. Fabris, G. Fratesi, R. Gebauer, U. Gerstmann, C. Gougoussis, A. Kokalj, M. Lazzeri, L. Martin-Samos, N. Marzari, F. Mauri, R. Mazzarello, S. Paolini, A. Pasquarello, L. Paulatto, C. Sbraccia, S. Scandolo, G. Sclauzero, A. P. Seitsonen, et al., *J. Phys.: Condens. Matter* **2009**, *21*, 395502.
[63] P. Giannozzi, O. Andreussi, T. Brumme, O. Bunau, M. Buongiorno Nardelli, M. Calandra, R. Car, C. Cavazzoni, D. Ceresoli, M. Cococcioni, N. Colonna, I. Carnimeo, A. Dal Corso, S. de Gironcoli, P. Delugas, R. A. DiStasio, A. Ferretti, A. Floris, G. Fratesi, G. Fugallo, R. Gebauer, U. Gerstmann, F. Giustino, T. Gorni, J. Jia, M. Kawamura, H.-Y. Ko, A. Kokalj, E. Küçükbenli, M. Lazzeri, et al., *J. Phys.: Condens. Matter* **2017**, *29*, 465901.
[64] J. P. Perdew, K. Burke, M. Ernzerhof, *Phys. Rev. Lett.* **1996**, *77*, 3865.
[65] P. E. Blöchl, *Phys. Rev. B* **1994**, *50*, 17953.
[66] G. Henkelman, B. P. Uberuaga, H. Jónsson, *J. Chem. Phys.* **2000**, *113*, 9901.